applied sciences

Article

An Improved Biomimetic Olfactory Model and Its Application in Traffic Sign Recognition

Jin Zhang *, Haobo He, Wei Li, Lid an Kuang, Fei Yu and Jiajia Zhao

College of Computer and Communication Engineering, Changsha University of Science and Technology, Changsha 410076, China
* Correspondence: mail_zhangjin@163.com; Tel.: +86-176-0731-0060

Abstract: In human and other organisms' perception, olfaction plays a vital role, and biomimetic olfaction models offer a pathway for studying olfaction. The most optimal existing biomimetic olfaction model is the KIII model proposed by Professor Freeman; however, it still exhibits certain limitations. This study aims to address these limitations: In the feature extraction stage, it introduces adaptive histogram equalization, Gaussian filtering, and discrete cosine transform methods, effectively enhancing and extracting high-quality image features, thereby bolstering the model's recognition capabilities. To tackle the computational cost issue associated with solving the numerical solutions of neuronal dynamics equations in the KIII model, it replaces the original method with the faster Euler method, reducing time expenses while maintaining good recognition results. In the decision-making stage, several different dissimilarity metrics are compared, and the results indicate that the Spearman correlation coefficient performs best in this context. The improved KIII model is applied to a new domain of traffic sign recognition, demonstrating that it outperforms the baseline KIII model and exhibits certain advantages compared to other models.

Keywords: olfaction; biomimetic olfaction models; feature extraction; pattern recognition; traffic sign recognition

Citation: Zhang, J.; He, H.; Li, W.; Kuang, L.; Yu, F.; Zhao, J. An Improved Biomimetic Olfactory Model and Its Application in Traffic Sign Recognition. *Appl. Sci.* **2024**, *14*, 87. https://doi.org/10.3390/app14010087

Academic Editors: Donald Y.C. Lie, Jian Xu and Chung-Chih Hung

Received: 30 October 2023
Revised: 12 December 2023
Accepted: 19 December 2023
Published: 21 December 2023

1. Introduction

Olfaction, as a fundamental sense in humans and other organisms, plays an essential role in many domains [1]. Biomimetic olfactory models, which emulate the principles and mechanisms of biological olfactory systems to simulate and understand the basic processes of olfactory perception, are a significant approach to studying olfaction. In this field, numerous biomimetic models of the olfactory neural system have emerged, demonstrating a wealth of variation and innovation. For example, the K-series models proposed by Professor Freeman, which evolved from K0, KI, and KII to KIII [2–5], realistically simulate the early stages of the olfactory neural system, including the olfactory epithelium, olfactory bulb, and olfactory cortex. Hopfield and Li [6] constructed an olfactory bulb model based on the biological anatomy and electrophysiological characteristics of the olfactory bulb and used the model for simulating the transformation process of odor information. Soh et al. [7] established an olfactory neural network model, which encapsulates the olfactory receptors, olfactory bulb, and piriform cortex and allows odor encoding in the olfactory bulb to be predicted by adjusting model parameters, as well as simulating the ability to extract features associated with "attention". The Li model [8] constructed by Li and colleagues focused on the olfactory bulb layer and olfactory cortex. Hans et al. [9], based on the laminar features of the olfactory cortex, subdivided it into three layers for construction. At a macro level, the model structure omits the simulation of olfactory receptors, but the rest corresponds to the actual structure of the olfactory neural tissue, and the model parameters are primarily grounded in experimental data from neurophysiology.

Among the multitude of biomimetic models, the KIII model, grounded in experimental data from neurophysiology, corresponds closely to the actual structure of the olfactory neural tissue and has demonstrated high similarity between its simulated brain waves and the outputs of the real olfactory neural system. The KIII model not only exhibits a high degree of biomimicry but has also shown good pattern recognition capabilities in applications. It has already been utilized in fields like tea leaf categorization [10], facial recognition [11,12], fabric texture identification [13], pre-processing filters [14], and electroencephalogram (EEG) recognition [15], showcasing its potential in pattern recognition and data processing. Although the KIII model excels in certain areas, there remain some issues worthy of attention: lengthy training times, suboptimal feature extraction abilities, and an overly simplistic decision-making approach.

This study aims to enhance the KIII model by addressing its current limitations and further improving its pattern recognition capabilities. Traffic sign recognition has become a prominent research focus in recent years, and traffic sign datasets adhere to specific standards and rules. This provides us with a robust testing scenario to assess the model's ability to handle diversity and complexity. For the KIII model, traffic sign recognition represents a novel application domain. Therefore, we choose to validate the feasibility of the optimized KIII model using a traffic sign dataset and compare it with the original baseline KIII model as well as other models.

2. The KIII Model

The KIII model is constructed based on the anatomical structure of the entire anterior olfactory neural pathway, and it exhibits a well-defined correspondence with the structure of the olfactory system. The K-series models consist of K0, KI, KII, and KIII, with K0 serving as the fundamental module. The KI model is composed of two K0 models, and the KII model is composed of two KI models. The K0, KI, and KII models are interconnected in a feedforward and delayed feedback manner to form the KIII model. As shown in Figure 1, the complete KIII model is divided into five layers: the periglomerular cell (PG) layer, the olfactory bulb (OB) layer, the anterior olfactory nucleus (AON) layer, the prepyriform cortex (PC) layer, and the external capsule (EC) layer. The following is the topological structure of the KIII model:

In the Figure 1, symbols and labels are used to represent different cell types and neuronal layers to provide a better description of the composition and functionality of the olfactory system. Specifically, the symbol '+' denotes excitation, while the symbol '-' denotes inhibition. 'R' is used to represent olfactory receptor cells responsible for perceiving and receiving odor information. 'P' represents the periglomerular cells connecting the olfactory bulb, which are part of the OB (olfactory bulb) layer. 'M' and 'G' denote excitatory mitral cells and inhibitory granule cells, respectively, together forming the KII model, which simulates the OB layer. Inhibitory 'I' and excitatory 'E' cells constitute the KII model, corresponding to the anterior olfactory nucleus (AON) layer. Additionally, inhibitory 'B' and excitatory 'A' cells form the KII model, corresponding to the prepyriform cortex (PC). 'C' represents deep pyramidal cells [6,13–15].

In the KIII model, each 'R' represents a K0 model, and 'n' parallel 'R' units constitute the n-channel input of the KIII model. The periglomerular cells 'P' preprocess signals from olfactory receptors 'R'. Mitral cells 'M' in the olfactory bulb layer (OB) receive signals from both periglomerular cells 'P' and olfactory receptors 'R' and transmit information to granule cells 'G'. Mitral cells 'M' excite granule cells 'G', while granule cells 'G' inhibit mitral cells 'M', forming a negative feedback oscillatory neural loop. After processing in the olfactory bulb layer OB, mitral cells 'M' transmit information to the anterior olfactory nucleus (AON) and the prepyriform cortex (PC) through the lateral olfactory tract (LOT). The anterior olfactory nucleus (AON) and the prepyriform cortex (PC) also contain excitatory neurons 'E' and 'A', as well as inhibitory neurons 'I' and 'B', forming similar oscillatory loops. The output signals from the prepyriform cortex (PC) reach the external capsule (EC) and provide feedback to the AON layer, OB layer, and PG layer through the 'Di' feedback mechanism. The oscillatory characteristics and negative feedback mechanism of these neural loops provide unique dynamic properties for odor signal processing.

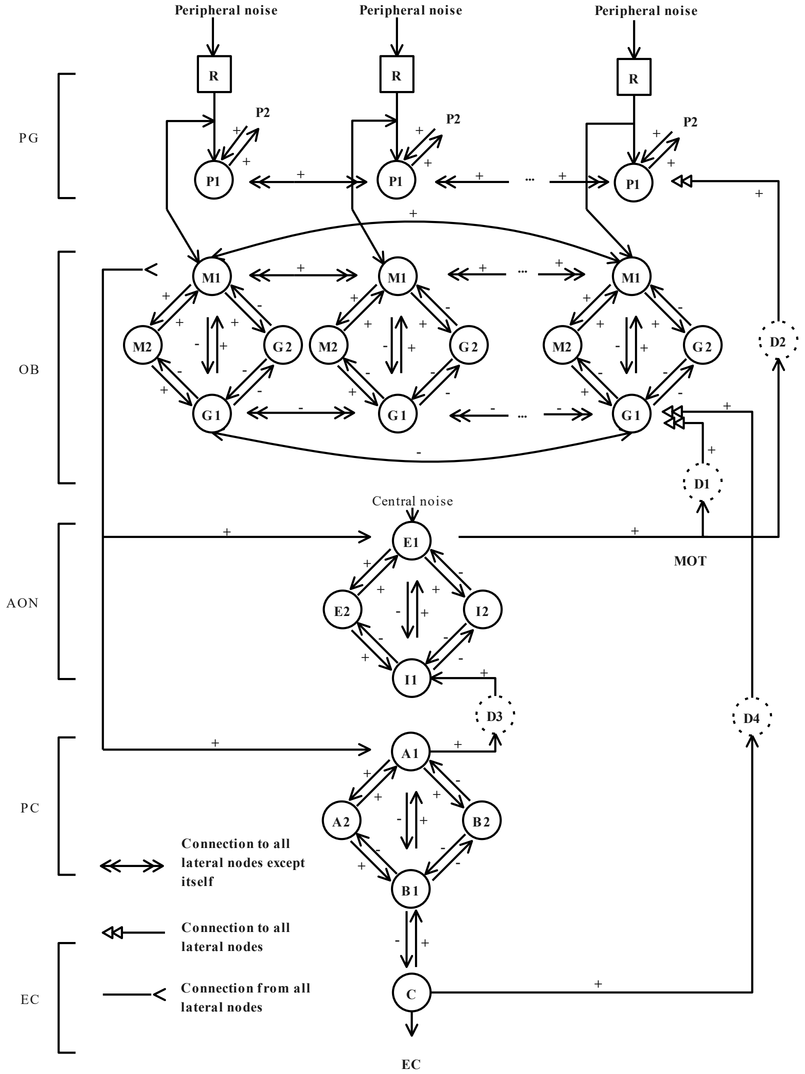

Figure 1. KIII model topology.

In the KIII model, the dataset is initially divided into training and testing sets in proportion. After preprocessing, the data is transformed into feature vectors and subsequently fed into 'N' channels. During this process, Hebbian learning is applied to extract the OB layer matrix, compute clustering centers for each class, and determine the weight parameters for each layer, which are then saved. Testing samples also undergo a similar process, leading to the calculation of a clustering center. In the decision layer, a similarity metric algorithm is employed to compare the testing center with the saved clustering centers, ultimately yielding the predicted class results. The overall process of training and testing in the KIII model is depicted in Figure 2.

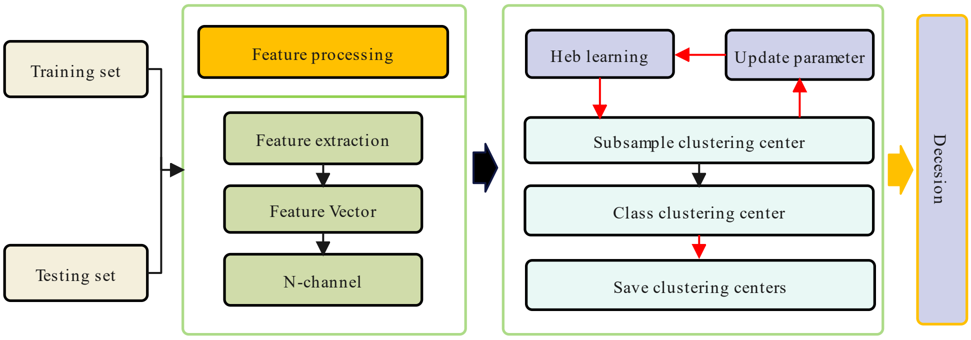

Figure 2. Experimental process. The red line represents the training process, the yellow line represents the feature extraction process, and the black line represents the common elements.

3. Problems and Improvement of KIII Model

3.1. Calculate the Cost

The establishment of the K-series models is based on the neural ensemble theory, where each node in the model is described by a common set of Equations (1)–(3):

$$\frac{1}{a \cdot b} \cdot [x_i''(t) + (a+b) \cdot x_i'(t) + a \cdot b \cdot x_i(t)] = \sum_{j \neq i}^{N} \Big[W_{ij} \cdot Q\Big(x_j(t), q_j\Big)\Big] + I_i(t) \quad (i = 1, \ldots, N) \tag{1}$$

$$Q(x_i(t), q) = \begin{cases} q \cdot (1 - e^{-\exp(x(t))-1}), & x(t) > x_0 \\ -1, & x(t) < x_0 \end{cases} \tag{2}$$

$$x_0 = ln(1 - q \cdot ln(1 + \frac{1}{q})) \tag{3}$$

where N represents the number of K0 units in the model's OB layer, that is, the number of model channels. $x_i(t)$ and $x_j(t)$ denote the potential state variables of the i-th and j-th neural ensembles, respectively. w_{ij} represents the synaptic connection strength from the j-th neuron to the i-th neural ensemble. $I_i(t)$ represents the external input received by the i-th neural ensemble. a and b are two time constants associated with neural electrophysiological activity, with experimental values of $a = 0.220$ and $b = 0.720$. $Q(x_j(t), q_j)$ is a non-linear S-shaped input/output function derived from the Hodgkin–Huxley (H-H) equation, where q represents the maximum asymptote of the sigmoid function. To solve the problem, we are given a second-order differential equation with initial values, and we seek the numerical solution for the function at the next time step. To facilitate the computation, we introduce intermediate variables and transform this second-order differential equation into two first-order differential equations, represented as Equations (4) and (5):

$$y''(t) + (a+b)y'(t) + aby(t) = abRHS(t) \tag{4}$$

$$\begin{cases} x_1(t) = y(t) \\ x_2(t) = y'(t) \end{cases} \Rightarrow \begin{cases} x_1'(t) = x_2(t) \\ x_2'(t) = abRHS(t) - (a+b)y'(t) - aby(t) \end{cases} \tag{5}$$

In the model, the initial time (t) is set to 0 with a step size of 1 ms, and at the 0 s mark, all neurons are in a resting state with the initial values of both first-order differential equations being 0. In the KIII model, a numerical solution must be computed for each pair of adjacent neurons at every moment. The baseline KIII model utilizes the fourth-order Runge–Kutta method, which undoubtedly incurs a significant computational cost. To balance precision and computing expenses, four numerical methods with varying degrees of accuracy were compared. These methods have different principles of solution, levels of computational precision, and execution times. Below is a brief introduction to these four methods.

3.1.1. Euler Method

Euler's method approximates the solution step by step by using initial values and the derivatives of the differential equation. It has a simple computational formula and is faster; however, due to its first-order accuracy, it may introduce errors in certain problems. Here is the Euler method's computational formula:

$$y_{n+1} = y_n + f(t_n, y_n) \cdot h \tag{6}$$

3.1.2. Trapezoidal Rule Method

The trapezoidal rule combines the ideas of Euler's method and the midpoint method by using the average of the derivatives at the current and next points in the update step. This reduces the numerical solution error caused by the estimation error of the derivatives, leading to a more accurate estimation of the derivatives. The calculation formula for the trapezoidal rule is as follows:

$$y_{n+1} = y_n + \frac{h}{2} \cdot (f(t_n, y_n) + f(t_{n+1}, y_{n+1})) \tag{7}$$

3.1.3. Third-Order Heun Method

The third-order Heun method belongs to the class of Runge–Kutta methods. Similar to Euler's method, Heun's method iteratively approaches the numerical solution of a differential equation. In comparison to the first-order Euler method, Heun's method maintains relative simplicity while achieving third-order accuracy in the numerical solution. It demonstrates good numerical stability and convergence. However, due to the involvement of two slope calculations, it incurs relatively higher computational costs. The calculation formula for the third-order Heun method is as follows:

$$\begin{cases} k_1 = f(t_n, y_n) \\ k_2 = f\left(t_n + \frac{h}{3}, y_n + \frac{h}{3} \cdot k_1\right) \\ k_3 = f\left(t_n + \frac{2h}{3}, y_n - \frac{h}{3} \cdot k_1 + h \cdot k_2\right) \\ y_{n+1} = y_n + \frac{h}{4} \cdot (k_1 + 3k_2 + k_3) \end{cases} \tag{8}$$

3.1.4. Fourth-Order Runge–Kuta Method

The fourth-order Runge–Kutta method utilizes a weighted average of multiple function values to approximate the numerical solution of a differential equation. The specific steps involve computing intermediate values and weighting coefficients to update the approximate values of the solution. Due to its use of more function values for approximation, it has a higher order, offering increased computational accuracy. However, it may require more computation time correspondingly. Below are the computational formulas for the fourth-order Runge–Kutta method:

$$\begin{cases} k_1 = f(t_n, y_n) \\ k_2 = f\left(t_n + \frac{h}{2}, y_n + h \cdot \frac{k_1}{2}\right) \\ k_3 = f\left(t_n + \frac{h}{2}, y_n + h \cdot \frac{k_2}{2}\right) \\ k_4 = f(t_n + h, y_n + h \cdot k_3) \\ y_{n+1} = y_n + \frac{h}{6}(k_1 + 2k_2 + 2k_3 + k_4) \end{cases} \tag{9}$$

3.2. Feature Extraction

The KIII model is inspired by the biological olfactory system and employs a biologically plausible feature extraction method. This method processes sensory data through the olfactory neural pathway, effectively capturing features such as texture and edges in one-dimensional sequences and simple images. One-dimensional sequences and simple images typically exhibit relatively simple structures, making them more amenable to feature extraction and pattern recognition. The KIII model performs well when dealing with one-dimensional sequences and simple images. However, its performance significantly deteriorates when applied to more complex and diverse images. Therefore, handling images and extracting features that represent original data effectively [16–18] is a challenging and critical task when using the KIII model for pattern recognition. In this study, in order to extract high-quality feature vectors, we incorporated previous research on image enhancement. In the feature extraction stage, we applied adaptive histogram equalization and Gaussian filtering to improve the overall image quality. Subsequently, we used gridded Discrete Cosine Transform (DCT) and a combination of global and local DCT to extract image features.

3.2.1. Adaptive Histogram Equalization

Based on previous research, a comparative analysis of image quality enhancement methods, such as Adaptive Histogram Equalization, Local Contrast Enhancement, Sharpening, Saturation Enhancement, and Dynamic Range Compression, has been conducted, as summarized in Table 1. Relative to other techniques, Adaptive Histogram Equalization displays a superior local contrast adjustment capability, which justifies the selection of this adaptive method in our study to more effectively manage local details in images, thus improving the overall image quality.

Table 1. Comparison of image quality enhancement methods.

Method	Advantages	Disadvantages
Adaptive Histogram Equalization	Performs histogram equalization based on the local characteristics, suitable for scenarios with uneven illumination within the image.	It may introduce noise, making the image appear over-processed.
Local Contrast Enhancement	Capable of highlighting local features of an image and enhancing detail.	It may result in the image looking overly sharp or processed, necessitating careful parameter adjustment.
Sharpening	Enhances the edges and details of an image.	It can potentially lead to noise or artifacts.
Dynamic Range Compression	Helps in preserving more details in the image, especially in high-contrast scenes.	The image may appear darker, requiring appropriate parameter adjustments to balance brightness and detail.

Adaptive Histogram Equalization (AHE) divides an image into small local regions and performs histogram equalization within each region. This process enhances the image's contrast while preserving its details and background information. This method takes into account the differences in brightness distribution in different regions of the image, ensuring that each local region's histogram is properly equalized, thus improving the visual quality of the image. In the case of Adaptive Histogram Equalization, the choice of key parameters can lead to different enhancement effects. Based on previous experimental research, this study sets the contrast enhancement limiting factor, clipLimit, to 1.0 and uses an 8×8 grid size, referred to as tileGridSize, to partition the image into local blocks.

3.2.2. Gauss Filter

Noise removal is an indispensable step in data processing, and for images, Gaussian noise is the most prominent and primary type of noise. Table 2 presents a comparative analysis of several common denoising methods. Considering the specific characteristics of the image, Gaussian filtering is ultimately selected as the method for this study.

Table 2. Comparison of denoising modes.

Method	Advantages	Disadvantages
Median Filtering	Effective for salt-and-pepper impulse noise, capable of removing extreme outliers; does not introduce additional sharpening effects.	It is not suitable for continuous noise like Gaussian noise; excessive denoising may lead to image blurring.
Bilateral Filtering	Preserves image edge information; has parameters to control the degree of smoothing, allowing for a balance between smoothing and denoising.	The computation is relatively slow; parameters need to be adjusted for optimal results.
Gaussian Filtering	Fast; effectively reduces Gaussian noise and smooths the image while preserving edge features of the image.	It may reduce the sharpness of the image and is not suitable for removing non-Gaussian noise.
Wiener Filtering	Capable of reducing noise while preserving image details; can adaptively filter based on the characteristics of noise.	It is sensitive to parameters, requiring accurate estimation of the statistical properties of the image and noise; the computation is complex.

Gaussian filtering, based on the concept of the Gaussian distribution, aims to reduce noise in images by applying a smoothing operation. It involves calculating a weighted average of the pixel values surrounding each pixel in the image, following a Gaussian distribution. This process effectively smooths the image and eliminates noise. While Adaptive Histogram Equalization can provide excellent image enhancement results, it may amplify noise in the image. Therefore, Gaussian filtering is chosen to process the image to minimize the noise impact introduced by histogram equalization. In Gaussian filtering, the size of the filter kernel determines the window size over which the filter slides on the image. In this study, a 5×5 Gaussian kernel size is used.

3.2.3. Feature Fusion Based on Discrete Cosine Transform

Feature extraction plays a crucial role in image processing and pattern recognition [19,20], enhancing model efficiency and performance by reducing data dimensions and preserving key information. In Table 3, we conducted a comparative analysis of various feature extraction methods. Due to the energy concentration property of the Discrete Cosine Transform (DCT), the representation of features becomes more compact, enabling better capture of essential characteristics in signals or images.

The Discrete Cosine Transform (DCT) decomposes an image into a weighted sum of a series of cosine functions, representing the image in the frequency domain. By separating high-frequency and low-frequency information, it provides a more compact representation of the image. Low-frequency coefficients reflect the overall structure, while high-frequency coefficients represent detailed information. Selecting appropriate frequency domain coefficients allows for the extraction of key features. DCT is a global feature extraction method, and its performance in extracting local features is relatively limited. To address this, we perform feature extraction in three steps:

1. Directly compute the DCT coefficients for the entire image as a representation of the whole image;

2. Divide the image into a grid and apply the Discrete Cosine Transform to each grid. Finally, aggregate the DCT coefficients from each grid to represent the entire image;
3. Concatenate the features obtained from steps 1 and 2, combining local features with global features to represent the entire image with richer features.

The overall process is illustrated in Figure 3.

Table 3. Comparative analysis of feature extraction methods.

Method	Advantages	Disadvantages
Local Binary Pattern	Simple and efficient; highly sensitive to texture features, suitable for texture analysis.	Not suitable for extracting object edges and shape features; unable to handle local detailed features.
Discrete Cosine Transform	Concentrates image energy on fewer coefficients; capable of capturing frequency domain features of signals.	Unable to capture image features containing sharp edges and details.
Histogram of Oriented Gradients	Exhibits good rotational invariance; provides a good description of object shapes and contours.	Relatively larger feature dimensions; sensitive to changes in lighting and viewpoint.

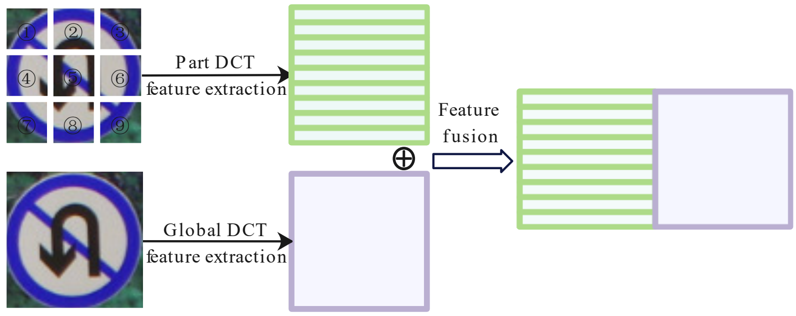

Figure 3. Feature fusion.

3.3. Measurement Mode

During the training phase, the KIII model saves the parameters for each layer and the cluster centers for each category. In the prediction phase, when a sample is input to the KIII model, it undergoes calculations to obtain a cluster center. This cluster center is then compared with all the saved cluster centers. The model calculates their similarity [21,22] and selects the cluster center with the highest similarity as the output category for that sample. The baseline KIII model uses the Euclidean distance to calculate similarity, which is somewhat simplistic. Therefore, we attempted to measure the similarity between two cluster centers from different perspectives by using four different methods: cosine similarity, covariance, Pearson coefficient, and Spearman coefficient. This allowed us to analyze the association between vectors from different angles and replace the original measurement method with the one that produced the best results.The following is a brief description of the centralized measures used in the experiment.

3.3.1. Euclidean Distance

The Euclidean distance measures the geometric distance between two vectors, which is the straight-line distance in a multidimensional space. It does not impose any specific requirements on data distribution but is sensitive to outliers. It is the default similarity measurement method used in the KIII model. For two points $A(a1, a2, \ldots, an)$ and $B(b1, b2, \ldots, bn)$ in an n-dimensional space, the Euclidean distance is calculated using the following formula:

$$D(A, B) = \sqrt{(A_{11} - B_{11})^2 + \ldots (A_{mn} - B_{mn})^2} = \sqrt{\sum_{i=1}^{m} \sum_{j=1}^{n} \left(A_{ij} - B_{ij}\right)^2} \quad (10)$$

3.3.2. Cosine Similarity

Cosine similarity assesses the degree of alignment between two vectors by calculating the cosine of the angle between them. It is commonly used with text data and high-dimensional sparse data. Cosine similarity is insensitive to the magnitude of the data and is suitable for high-dimensional data. However, it cannot capture relationships beyond linear ones and is not suitable for data containing negative values. The formula for calculating cosine similarity is as follows:

$$\text{Cos Sim}(A, B) = \frac{\sum_{i=1}^{m} \sum_{j=1}^{n} A_{ij} \cdot B_{ij}}{\sqrt{\sum_{i=1}^{m} \sum_{j=1}^{n} A_{ij}^2} \cdot \sqrt{\sum_{i=1}^{m} \sum_{j=1}^{n} B_{ij}^2}} \quad (11)$$

3.3.3. Covariance

Covariance is a statistical measure of the strength and direction of the linear relationship between two variables. For two vectors, covariance quantifies the overall strength and direction of their linear relationship, and it is sensitive to the scale of the data, unable to eliminate dimensional effects. For two variables, A and B, the formula for calculating covariance is as follows:

$$\text{Cov}(A, B) = \frac{1}{n-1} \sum_{i=1}^{n} (A_i - \bar{A})(B_i - \bar{B})^T \quad (12)$$

Here, n represents the number of samples, A_i and B_i represent the i-th dimension of matrices A and B, respectively, and $\bar{A}$ and $\bar{B}$ represent the sample means of matrices A and B, respectively.

3.3.4. Pearson Correlation Coefficient

The Pearson correlation coefficient measures the strength of the linear relationship between two variables. It is widely used in statistics to quantify the strength and direction of a linear relationship. However, it has certain requirements regarding data scale and normality and is not suitable for capturing nonlinear relationships. The formula for calculating the Pearson correlation coefficient is as follows:

$$\rho(A, B) = \frac{\text{cov}(A, B)}{\sigma A \cdot \sigma B} \quad (13)$$

Here, cov(A, B) represents the covariance of vectors A and B, and σA and σB represent the standard deviations of A and B.

3.3.5. Spearman's Rank Correlation Coefficient

The Spearman's rank correlation coefficient measures the rank correlation between two variables. Its calculation is based on the ranks of the variables rather than their specific numerical values. Therefore, it is suitable for situations involving non-linear relationships, ordered data, or the presence of outliers, but it cannot capture linear relationships. It is not suitable for continuous numerical data. The formula for calculating the Spearman's rank correlation coefficient is as follows:

$$\rho(A, B) = 1 - \frac{6 \sum_{i=1}^{n} d_i^2}{n(n^2 - 1)} \quad (14)$$

Here, d represents the rank difference of variables, n represents the number of samples and in this paper refers to the length of the first dimension of the cluster center vector.

For the five aforementioned measurement methods, their ranges and the relationship between their values and correlation are presented in Table 4.

Table 4. The relationship between different measurement methods and correlation.

Method	Value Range	Relationship with Similarity
Euclidean Distance	$D(A, B) \in [0, +\infty)$	The smaller the value of $D(A, B)$ the greater the similarity between vectors A and B.
Cosine Similarity	$CosSim(A, B) \in [-1, 1]$	1 indicates complete similarity, -1 indicates complete dissimilarity, and 0 denotes no correlation.
Covariance	$Cov(A, B) \in (-\infty, +\infty)$	The greater the absolute value of $Cov(A, B)$, the stronger the correlation.
Pearson Correlation Coefficient	$\rho(A, B) \in [-1, 1]$	1 represents perfect positive correlation, -1 represents perfect negative correlation, and 0 represents no correlation.
Spearman's Rank Correlation Coefficient	$\rho(A, B) \in [-1, 1]$	1 represents perfect positive correlation, -1 represents perfect negative correlation, and 0 represents no correlation.

4. Experiment and Result Analysis

The experimental dataset used in this study is the TSRD dataset from the Chinese Traffic Sign Database, and the task is classification recognition. Based on prior research on KIII pattern recognition, the currently employed KIII model still exhibits certain limitations in terms of performance. Due to this, the dataset size should not be too large. In this case, 20 images were selected for each category, and there are a total of 58 categories. A portion of the data is shown in Figure 4.

Figure 4. Partial data display.

To comprehensively evaluate the feasibility of improving the KIII model, three datasets of different sizes were selected during the experimental process, each corresponding to one of the three different channels of the KIII model. During the training process, a partitioning strategy with a 60% training set and a 40% test set was employed to ensure the full utilization of data. The number of iterations was set to 1, and the experimental development environment included a CPU I5-13600KF and a GPU RTX 4080 16 GB, running Python 3.9.

4.1. Comparison before and after Improvement to the KIII Model

The figure below depicts the total time spent on training and testing the KIII model for three different original image sizes (corresponding to three different channels of the KIII model) using four different numerical methods: Euler's method, the trapezoidal rule method, the third-order Heun method, and the fourth-order Runge–Kutta method for calculating the numerical solutions of a system of differential equations. The figure also presents the average recognition accuracy on the test dataset for each numerical method.

According to the results shown in Figures 5 and 6, training with different numerical methods resulted in minimal differences in test accuracy, with an average accuracy difference of less than 1%. However, there was a significant fivefold difference in time expenditure, indicating that the KIII model's pattern recognition task does not demand strict precision in numerical solution accuracy for the next time step. This also highlights the notable advantage of Euler's method in terms of time efficiency when solving numerical solutions. Additionally, it is evident that the KIII model exhibits poor recognition performance on untreated complex images, with an average accuracy of only 56.69%. Therefore, image processing and feature extraction are necessary and critical for improved performance.

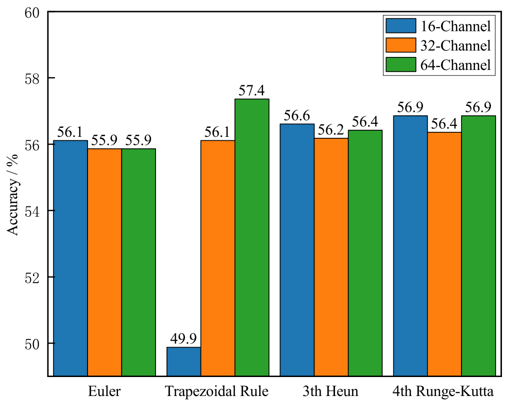

Figure 5. Accuracy of different solution methods.

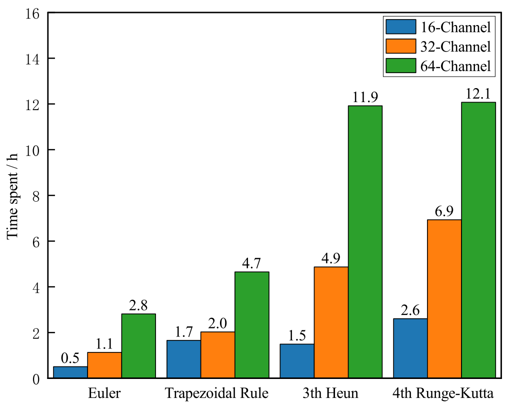

Figure 6. Time spent on different solution methods.

The following figure shows the recognition results of image data of three different sizes after applying adaptive histogram equalization, Gaussian filtering, and the fusion of global and local DCT features introduced in Section 3.2 during the feature extraction stage of the KIII model. The Euler method is used for solving the differential equations, and the experimental results are as shown in the following figure.

According to the results in Figures 7 and 8, introducing a new feature extraction methods in the KIII model significantly improved the model's performance compared to previous iterations, demonstrating the rationale behind these methods. Adaptive Histogram Equalization enhances the uniformity of the grayscale distribution in original images, effectively highlighting fine details as the image's information entropy increases. Gaussian filtering reduces image noise, resulting in a smoother image. Despite the increased computational cost due to the extraction and combination of local and global image features, the average test accuracy reached 89.10%. This represents a notable 32.41%

improvement over the KIII model's direct recognition of the original images. Taking all factors into consideration, the proposed feature extraction methods have shown significant effectiveness in pattern recognition tasks for the KIII model.

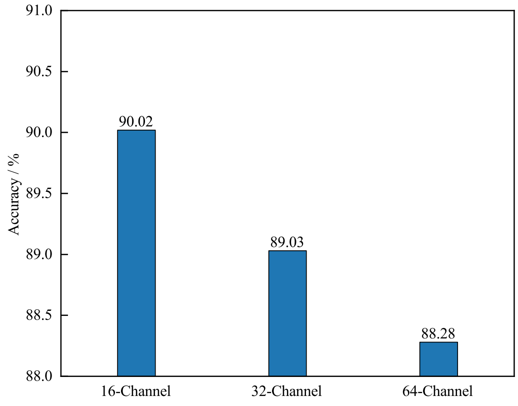

Figure 7. Accuracy after feature extraction.

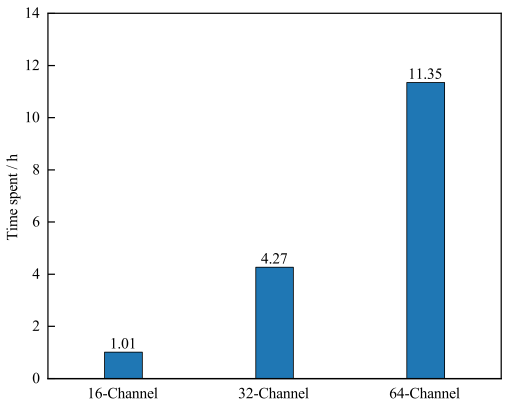

Figure 8. Time spent after feature extraction.

Finally, experiments were conducted regarding the correlation measurement methods described in Section 3.3 at the model decision stage, and the results are shown in Figure 9.

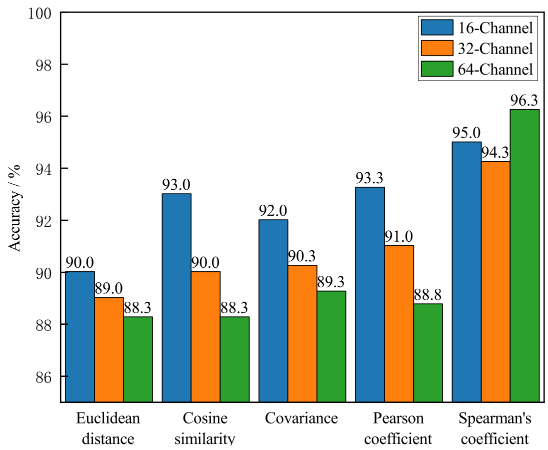

Figure 9. Accuracy of different decision-making methods.

According to the results shown in Figure 9, the performance of the Spearman correlation coefficient in the decision-making stage is significantly superior to other measurement methods. This can be attributed to several factors. Firstly, the Spearman correlation coefficient exhibits better adaptability to non-linear relationships, a crucial characteristic given that similarity relationships among traffic signs are non-linear due to varying shooting angles, lighting conditions, and deformations. Secondly, the Spearman correlation coefficient demonstrates robustness against outliers, which is essential in real-world scenarios where images may contain outliers due to factors such as lighting, dirt, and damage. Thirdly, since traffic sign categories often follow certain logical or rule-based orderings, the Spearman correlation coefficient effectively preserves this sequential information. Therefore, we replace the Euclidean distance in the baseline KIII model with the Spearman correlation coefficient for decision making.

Additionally, it can be observed that as the number of input image channels increases, the model's test accuracy exhibits a declining trend. This is because, with larger sample sizes, the feature vectors also increase in size, requiring the model to learn more features. This undoubtedly adds to the model's burden, leading to a decrease in accuracy.

4.2. Comparison with Other Models

The ultimate goal of artificial intelligence is to endow machines with learning and decision-making capabilities similar to humans. Therefore, the performance and biomimicry of models are equally important. In addition to comparing the improved KIII model's results with the baseline KIII model, we contrast the experimental outcomes with recognition results from other models, as shown in Table 5. The experiments indicate that, although the KIII model slightly lags behind other models in terms of performance, it exhibits a significant advantage in biomimicry. Moreover, it achieves outstanding results after a single learning iteration, much like the strong learning ability of the biological olfactory neural system in response to new odors.

Table 5. KIII compared to other models.

Model	Iterations	Channels (Image Size)	Biomimetic Degree	Average Accuracy
AlexNet	100	64	low	93.1%
RIECNN [23]	100	64	low	96.9%
CapsNetCNN [24]	100	64	low	97.5%
Improved KIII	1	64	high	95.2%

4.3. Conclusions and Prospects

This study aimed to improve the baseline KIII model. We delved into the trade-off between the accuracy and time expenditure of solving differential equations in the KIII model. The results showed that the Euler method consumes minimal time and achieves decent recognition performance. To address the KIII model's weakness in recognizing disordered signals, we introduced image enhancement and feature extraction methods in the feature extraction stage, resulting in the extraction of richer features. We validated their significant contribution to the model's recognition performance in experiments.

In the model decision stage, we compared five measurement algorithms, and the results indicated that the Spearman rank correlation coefficient outperformed other metrics. Finally, we applied the improved KIII model to a new application domain—traffic sign recognition. On the TSRD dataset, the improved KIII model achieved a recognition rate of 95.18%, which was comparable to other classical models, demonstrating the feasibility of the improvement.

In future research, we will focus on the following aspects:

- From a performance perspective, we will draw inspiration from deep learning concepts. For instance, we will adjust the connection methods between neurons in the model from existing connections to local or random connections. We may also integrate classical modules from deep learning into the KIII model to enhance its performance and explore the applications of Convolutional Neural Networks and Recurrent Neural Networks as they possess distinct advantages in handling spatial and temporal data, respectively. These advanced neural network architectures may play a crucial role in the analysis of olfactory data.

- From a biomimetic perspective, we will explore whether the model's structure, compared to the anatomical structure of the real olfactory neural system, can be further improved to increase its biomimicry.
- Efforts will be made to expand the application of the KIII model into additional domains, particularly in areas related to olfaction.

Author Contributions: Methodology, H.H.; Validation, H.H.; Resources, W.L.; Writing—original draft, H.H.; Writing—review & editing, W.L.; Supervision, L.K., F.Y. and J.Z. (Jiajia Zhao); Project administration, J.Z. (Jin Zhang); Funding acquisition, J.Z. (Jin Zhang). All authors have read and agreed to the published version of the manuscript.

Funding: This research was funded by the Natural Science Foundation of Hunan Province (2021JJ30456, 2021JJ30734), the Open Research Project of the State Key Laboratory of Industrial Control Technology (No. ICT2022B60), the National Defense Science and Technology Key Laboratory Fund Project (2021-KJWPDL-17), the National Science Foundation of China (61972055), and the Research Foundation of Education Bureau of Hunan Province, China (20C0030).

Institutional Review Board Statement: Not applicable.

Informed Consent Statement: Not applicable.

Data Availability Statement: In this study, we used a public datasets: The TSRD, which is available at http://www.nlpr.ia.ac.cn/pal/trafficdata/recognition.html/ (accessed on 18 December 2023).

Conflicts of Interest: The authors declare no conflict of interest.

References

1. Firestein, S. How the olfactory system makes sense of scents. *Nature* **2001**, *413*, 211–218. [CrossRef] [PubMed]
2. Chang, H.J.; Freeman, W.J. Parameter optimization in models of the olfactory neural system. *Neural Netw.* **1996**, *9*, 1–14. [CrossRef]
3. Chang, H.J.; Freeman, W.J.; Burke, B.C. Biologically modeled noise stabilizing neurodynamics for pattern recognition. *Int. J. Bifurc. Chaos* **1998**, *8*, 321–345. [CrossRef]
4. Le, W. Research and Application of Neural Model of Olfactory System. Master's Thesis, Zhejiang University, Hangzhou, China, 2005.
5. Souza, F.; Antunes, G. Investigating the properties of adaptation in a computational model of the olfactory sensory neuron. *Neurocomputing* **2007**, *70*, 1663–1667. [CrossRef]
6. Li, Z.; Hopfield, J.J. Modeling the olfactory bulb and its neural oscillatory processings. *Biol. Cybern.* **1989**, *61*, 379–392. [CrossRef] [PubMed]
7. Soh, Z.; Tsuji, T.; Takiguchi, N.; Ohtake, H. Neuro-based olfactory model for artificial organolep-tic tests. *Artif. Life Robot.* **2009**, *14*, 474–479. [CrossRef]
8. Li, Z.; Hertz, J. Odor recognition and segmen-tation by coupled olfactory bulb and cortical networks. *Neurocomputing* **1999**, *26*, 789–794. [CrossRef]
9. Liljenstrom, H. Modeling the dynamics of olfactory cortex using simplified network units and realistic architecture. *Int. J. Neural Syst.* **1991**, *2*, 1–15. [CrossRef]
10. Yang, X.; Fu, J.; Lou, Z.G.; Wang, L.Y.; Li, G.; Freeman, W. *Tea Classification Based on Artificial Olfaction Using Bionic Olfactory Neural Network*; Springer: Berlin/Heidelberg, Germany, 2006; Volume 3973, pp. 343–348.
11. Li, G.; Zhang, J.; Wang, Y.; Freeman, W. Face recognition using a neural network simulating olfactory systems. *Lect. Notes Comput. Sci.* **2006**, *3972*, 93–97.
12. Carlos, L.; Rosa, J. Face recognition through a chaotic neural network model. In Proceedings of the 2014 International Joint Conference on Neural Networks (IJCNN), Beijing, China, 6–11 July 2014; pp. 859–863.
13. Bao, X.; Cao, Z.; Wang, Y.; Zhou, Y.; Zhu, H. Textile weave recognition based on olfactory neural network. *Text. J.* **2011**, *32*, 52–56.
14. Garcia Rosa, J.L.; Piazentin, D.R.M. A new cognitive filtering approach based on freeman k3 neural networks. *Appl. Intell. Int. J. Artif. Intell. Neural Netw. Complex Probl. -Solving Technol.* **2016**, *45*, 363–382. [CrossRef]
15. Hu, R.; Guang, L.; Jin, Z. A new method for EEG feature extraction. *Chin. J. Sci. Instrum.* **2006**, *3*, 2187–2188.
16. Jiang, J.; Subakti, H.; Liang, H.S. Fingerprint feature extraction for indoor localization. *Sensors* **2021**, *21*, 5434. [CrossRef] [PubMed]
17. Huang, W.; Wang, Y.; Yang, J.; Xu, Y. Stance Detection Based on User Feature Fusion. *Comput. Intell. Neurosci.* **2022**, *2022*, 5738404. [CrossRef] [PubMed]
18. Ni, J.; Sun, H.; Xu, J.; Liu, J.; Chen, Z. A feature aggregation and feature fusion network for retinal vessel segmentation. *Biomed. Signal Process. Control* **2023**, *85*, 104829. [CrossRef]

19. Entezami, A.; Hassan, S.; Bahareh, B. A novel double-hybrid learning method for modal frequency-based damage assessment of bridge structures under different environmental variation patterns. *Mech. Syst. Signal Proces.* **2023**, *201*, 110676. [CrossRef]
20. Entezami, A.; Hassan, S.; Bahareh, B. Long-term health monitoring of concrete and steel bridges under large and missing data by unsupervised meta learning. *Eng. Struct.* **2023**, *279*, 115616. [CrossRef]
21. Wang, Z.; Chen, J.; Hu, J. Multi-View Cosine Similarity Learning with Application to Face Verification. *Mathematics* **2022**, *10*, 1800. [CrossRef]
22. Kirisci, M. New cosine similarity and distance measures for Fermatean fuzzy sets and topsis approach. *Knowl. Inf. Syst.* **2023**, *65*, 855–868. [CrossRef]
23. Abdel-Salam, R.; Mostafa, R.; Abdel-Gawad, A.H. RIECNN: Real-time image enhanced CNN for traffic sign recognition. *Neural Comput. Appl.* **2022**, *34*, 6085–6096. [CrossRef]
24. He, S.H.; Chen, L.; Zhang, S.Y.; Guo, Z.; Sun, P.; Liu, H.; Liu, H. Automatic recognition of traffic signs based on visual inspection. *IEEE Access* **2021**, *9*, 43253–43261. [CrossRef]